Applied Catalysis B: Environmental 193 (2016) 16–21

Contents lists available at ScienceDirect

Applied Catalysis B: Environmental

journal homepage: www.elsevier.com/locate/apcatb

Carbon quantum dots decorated Bi_2WO_6 nanocomposite with enhanced photocatalytic oxidation activity for VOCs

Xufang Qian, Dongting Yue, Zheyi Tian, Meng Reng, Yao Zhu, Miao Kan, Taiyang Zhang, Yixin Zhao*

School of Environmental Science and Engineering, Shanghai Jiao Tong University, 800 Dongchuan Rd., Shanghai 200240, China

ARTICLE INFO

Article history:
Received 11 March 2016
Received in revised form 2 April 2016
Accepted 5 April 2016
Available online 6 April 2016

Keywords:
Photocatalysis
VOCs
CQDs
Bi_2WO_6

ABSTRACT

We incorporated highly stable carbon quantum dots (CQDs) with Bi_2WO_6 to sufficiently photocatalytic removal of gaseous volatile organic compounds (VOCs) utilize solar energy. With the facile decoration of CQDs, the composite photocatalysts of CQDs/Bi_2WO_6 extend the absorption into visible light region and improve the photoexcited charge separation in comparison with pristine Bi_2WO_6. The CQDs/Bi_2WO_6 exhibited higher photocatalytic oxidation activities towards acetone and toluene under both UV–vis and visible light irradiation. In all, CQDs could be a promising candidate for visible light photocatalysts due to their superior ability to extend the visible absorption and suppress the photo-excited charge recombination.

1. Introduction

Volatile organic compounds (VOCs) are among the most harmful pollutants in air and result in outdoor and indoor air deterioration [1,2]. Accordingly, the elimination of VOCs has always attracted much attention in pollutants control. Various strategies including physical adsorption, chemical absorption, catalytic combustion and biological treatment have been used in VOCs control. Photocatalytic oxidation (PCO) has been widely investigated as a mild and clean advanced oxidation technology candidate [3–5]. The key steps of PCO process is to photogenerate highly active photo-exited e^-/h^+ pairs and separate the charge for photocatalytic reaction. The high oxidation potential of h^+ and the active intermediates produced by complicated reactions in the presence of e^-/h^+ is the important driving force in PCO process of VOCs under light irradiation.

Typical and classic photocatalyst of TiO_2 has been widely used for PCO of organic pollutants in water and air under UV irradiation [6–9]. However, the limited utilization of 3–5% UV light of solar energy for TiO_2 photocatalyst become one of the fatal obstacles in practical application. Accordingly, visible light photocatalysts are desired for PCO treating of toxic pollutants. Bi_2WO_6 with band gap of 2.69 eV possesses orthorhombic Aurivillius-type structure, which can be excited by visible light and showed PCO performance for organic pollutants in air and water [10–12]. However, the photocatalytic performance of Bi_2WO_6 is limited due to the weak light absorbance and fast charge recombination which is a stubborn shortcoming for both of TiO_2 and Bi_2WO_6. In order to effectively improve the PCO performance of Bi_2WO_6, several methods according to the principle of enhancing the light harvesting and improving the e^-/h^+ separation have been adopted. For example, the most widely used method is to construct photocatalytic heterojunctions including Bi_2WO_6-carbon and Bi_2WO_6-semiconductor heterostructures [13–19]. In regard to Bi_2WO_6-carbon composite photocatalysts, graphitic carbon based materials with delocalized conjugated π system such as carbon nanotube (CNT), graphene, fullerene (C60), and carbon nitride (C_3N_4) were incorporated with Bi_2WO_6 semiconductor to increase the photo-excited charge separation and inhibit the recombination [20–23].

Monodispersed carbon quantum dots (CQDs) with graphite structure and diameter of 2–10 nm have many unique properties, such as optical absorption in UV and near-visible region, photo-induced electron transfer, photoluminescence, and electron reservoir properties, which makes it become a promising candidate for photocatalysis application. CQDs have been employed in combining with hematite, BiOX (X = Br, Cl) [24,25], Bi_2WO_6 [26], $BiVO_4$ [27], C_3N_4 [28], Ag_3PO_4 [29], TiO_2 [30] for PCO of organic pollutants in aqueous solution. However, PCO performance of VOCs has never been tested upon CQDs/semiconductor composite photocatalysts by UV and visible light irradiation and O_2. Since the PCO process of VOCs was supposed to occur at the interface of

* Corresponding author.
E-mail address: yixin.zhao@sjtu.edu.cn (Y. Zhao).

http://dx.doi.org/10.1016/j.apcatb.2016.04.009
0926-3373/

photocatalytic sites and adsorbed VOCs molecules [31–33], CQDs with sp^2-hybridized graphitic structures and hydrophilic hydroxyl, carboxyl groups were supposed to be an excellent candidate for accumulation of VOCs around CQDs for the photocatalytical mineralization of VOCs into nontoxic CO_2 and H_2O. Herein, CQDs/Bi_2WO_6 heterostructure was fabricated and employed in PCO of representative VOCs i.e. acetone and toluene under UV and visible light irradiation. With the decoration of CQDs, the CO_2 production from VOCs mineralization was greatly increased in comparison with pristine Bi_2WO_6 under both UV and visible light irradiation.

2. Experiment

2.1. Chemicals

Bismuth (III) nitrate pentahydrate ($Bi(NO_3)_3{\cdot}5H_2O$), tungstic acid sodium salt (Na_2WO_4), acetic acid (CH_3COOH), ethanol, acetone and toluene were of analytical purity and were used as received. All of them were purchased from Sinopharm Chemical Reagent Co., Ltd. Polyvinylpyrrolidone (PVP) and magnesium sulfate were purchased from Aladdin Industrial Corporation.

2.2. Materials synthesis

2.2.1. Hydrothermal synthesis of Bi_2WO_6

In a typical synthesis, 0.55 g (1.66 mmol) Na_2WO_4 and 0.011 g PVP were dissolved in deionized (DI) water to obtain a clear aqueous solution under ultrasonic treatment for 30 min. Then, 1.617 g (3.32 mmol) $Bi(NO_3)_3{\cdot}5H_2O$ was dissolved in CH_3COOH with vigorous stirring, followed by mixing the above two solutions and stirring until the mixture became homogeneous. The obtained mixture was transferred into a 150 mL of Teflon-lined stainless steel autoclave, which was maintained at 150 °C for 18 h. The precipitate was obtained by centrifuging and repeatedly washing with ethanol and DI water several times, followed by drying at 60 °C for 6 h.

2.2.2. Electrochemical synthesis of CQDs

CQDs were synthesized by an alkali-assisted electrochemical method [34]. In a typical synthesis, 1.2 g NaOH was dissolved in 63 mL H_2O/ethanol (1:20) mixture solution, which were treated under ultrasonic for several minutes to yield a transparent solution. Afterwards, two graphite rods (0.5 cm in diameter) were inserted into the solution as the anode and cathode, respectively. A brown solution was then produced under 30 V. The crude CQDs solution was treated with $MgSO_4$ and stirred slowly for 24 h to remove the water and salts. The obtained transparent CQDs solution was separated with a dialysis bag (3500 Da) and a deep orange solution was collected and stored for use.

2.2.3. Loading of CQDs on Bi_2WO_6

CQDs/$BiWO_6$ composites were prepared through a facile wet impregnation method. 0.2 g Bi_2WO_6 was dispersed into 10 mL ethanol, followed by adding 1.0–6.0 g of CQDs stock solution under ultrasonic. Subsequently, the ethanol solvent was removed by rotating evaporation method at 35 °C, followed by drying at 40 °C in vacuum overnight. The resulting photocatalysts were designated as CQDs(x)/$BiWO_6$ in which x (1–6) represents the mass of CQDs stock solution.

2.3. Characterization

Powder XRD patterns were recorded on a Shimadzu XRD-6100 diffractometer with Cu Kα radiation. The data were recorded at a scan rate of 10/min. Field-emission scanning electron microscopy (FESEM) measurements were performed on a JSM-7800F Prime scanning electron microscope. Fourier transform infrared (FTIR) spectra of the samples were measured on Tensor 27 FTIR spectrometer (Nicolet 6700). Samples were diluted with KBr and compressed into thin pellets. Diffuse reflectance spectra (DRS) were measured using a Lambda 750 UV–vis-NIR (ultraviolet–visible-near-infrared) spectrophotometer. $BaSO_4$ was used as the reflectance standard material. Surface electronic states were analyzed by XPS (PerkinElmer PHI 5000C, AlKa). All binding energies were calibrated by using the contaminant carbon (C 1s = 284.6 eV) as a reference. Transmission electron microscopy (TEM) micrographs were obtained using a JEOL-JEM-2010 microscope (JEOL, Japan). The transient photocurrent responses were measured in a quartz cell with a conventional three-electrode system on an electrochemical workstation (CHI660E, CHENHUA Instrument Company).

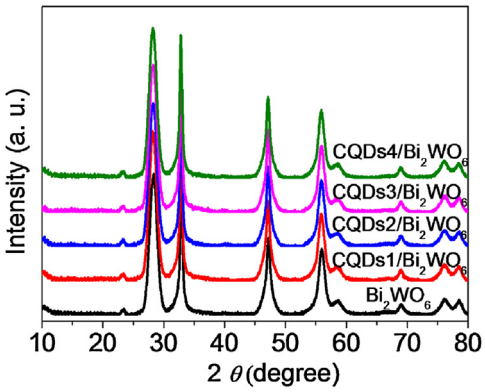

Fig. 1. XRD diffraction patters of pristine Bi_2WO_6 and CQDs decorated Bi_2WO_6 nanoflake aggregates.

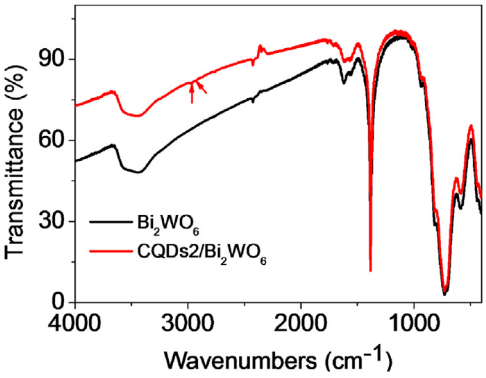

Fig. 2. FTIR spectra of pristine Bi_2WO_6 and CQDs4/Bi_2WO_6.

2.4. Photocatalytic degradation of VOCs

Photocatalytic degradation of gaseous VOCs were performed under visible light with a 420 nm cut filter and UV–vis light irradiation using 500 W xenon lamp (CEL-HXF300). The distance of light source to the window of reactor is 2 cm (~400 mW/cm^2). A self-developed pryrex reactor (total volume of 250 mL) with a flat quartz window on the top were used, wherein 0.02 g photocatalyst were mixed with inert SiO_2 (0.48 g) and the mixture were loaded on a filter film placed in the bottom of the reactor. The reactors were sealed and flushed with O_2 for 30 min, and then 5 μL of liquid acetone (or toluene) were injected into the reactor and vaporized into gas phase. Before the lamp was switched on, the gas-solid adsorption equilibrium reached after 30 min. The photocatalytic oxidation of VOCs were evaluated by CO_2 detection at different time interval on gas chromatography (GC7900 equipped with a flame ionization detector (FID) & methane reforming furnace). The organic pollutants and intermediates were detected during the reaction

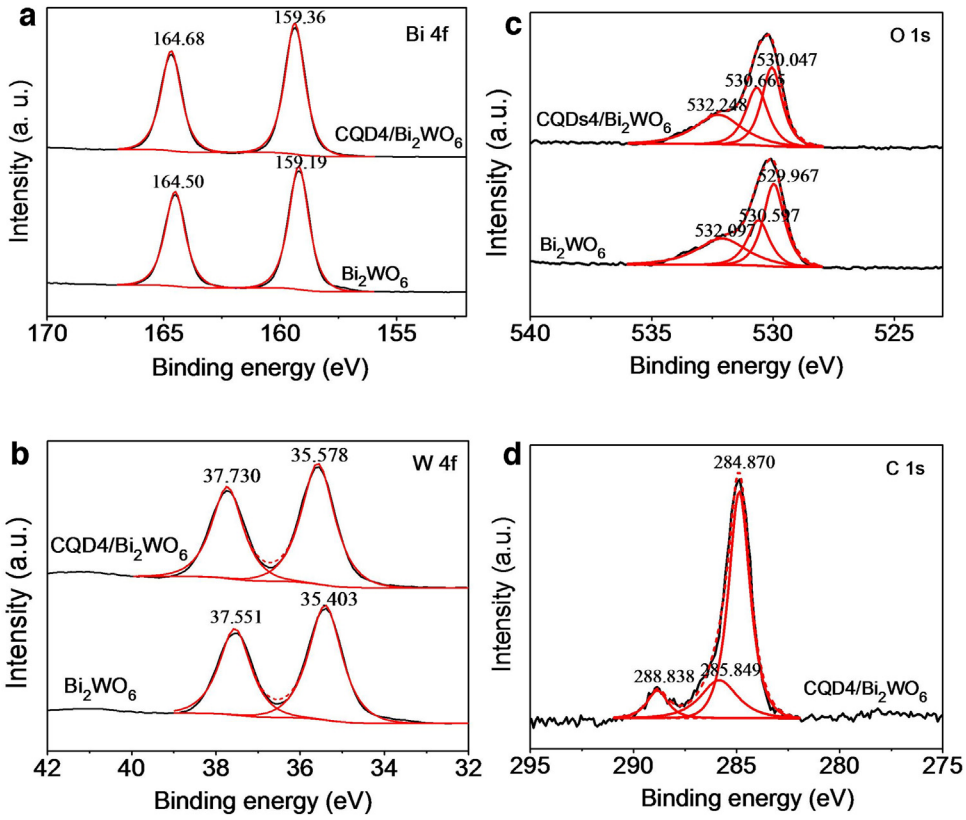

Fig. 3. High resolution XPS spectra of Bi 4f (a), W 4f (b), O 1s (c) and C 1s (d) for pristine Bi_2WO_6 and CQDs2/Bi_2WO_6, respectively.

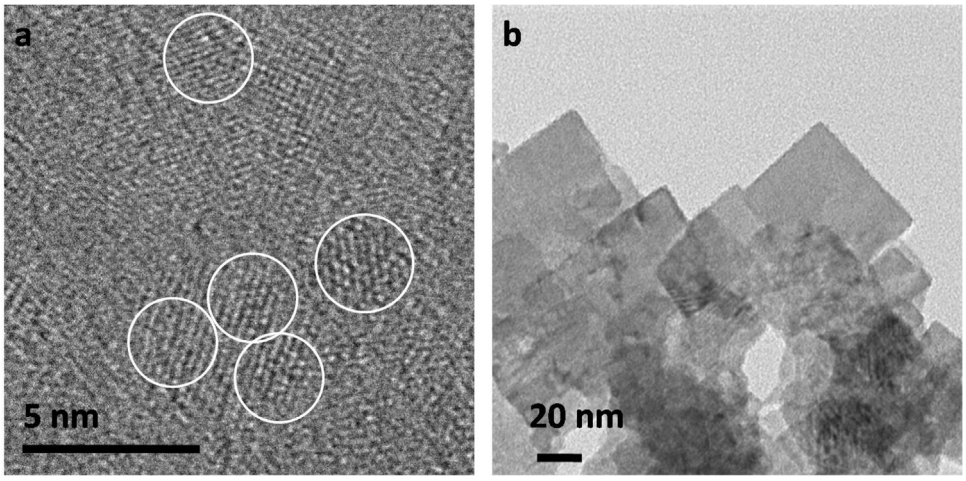

Fig. 4. TEM image of magnified CQDs (a) and CQDs decorated Bi_2WO_6 nanoflake aggregates (CQDs4/Bi_2WO_6, b).

on gas chromatography (GC-14B) equipped with an FID detector and capillary column (EN-5, 5% phenyl 95% dimethyl polysiloxane, 30 m × 0.32 mm × 0.25 μm).

3. Results and discussions

Pristine Bi_2WO_3 nanoflake aggregates exhibit typical diffraction peaks indexed to the orthorhombic phase of Bi_2WO_3 (JCPDS card no. 73–1126) (Fig. 1). No impurity diffraction peaks were observed which indicates the phase purity of Bi_2WO_3. After decoration of CQDs, the characteristic diffraction peaks of Bi_2WO_3 keep unchanged with increasing the mass contents of CQDs indicating the negligible effect on crystalline structure with CQDs decoration by a gentle wet impregnation process. On the other hand, none of new diffraction peaks appears which indicates the low content of CQDs on Bi_2WO_6. FTIR spectra of CQDs2/Bi_2WO_6 (Fig. 2) show two characteristic but weak peaks at 2973, 2910 cm^{-1} assigned to the skeletal vibration of C—H bond of CQDs, which are absence for pristine Bi_2WO_6 [35]. The strong and broad peaks at 3500 cm^{-1} and relatively weak peaks at 1624 cm^{-1} can be assigned to the stretching vibration and bending vibration of surface O—H bond, and the peak at 1624 cm^{-1} becomes weaker with CQDs, indicating the decoration of CQDs consumes partial surface O—H groups. The strong absorption peaks centered at 589, 730, 1382 cm^{-1} are assigned to stretching vibration of Bi—O, W—O and W—O—W bridging stretching modes, respectively [36]. The above results

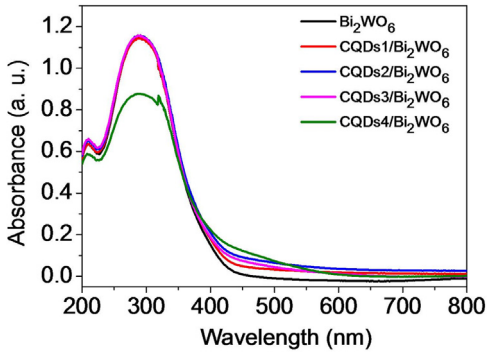

Fig. 5. UV–vis DRS spectra of pristine Bi_2WO_6 and CQDs decorated Bi_2WO_6 nanoflake aggregates.

manifest the composition of Bi_2WO_6 and presence of a small amount of CQDs.

XPS survey spectra were used to detect the electronic structures of Bi_2WO_6 and CQDs. The binding energy of all the element were calibrated with C 1s of aliphatic carbon at 284.6 eV. The full scan spectra of pristine Bi_2WO_6 and CQDs2/Bi_2WO_6 shows the presence of elements Bi, W, O and C (Fig. S1). The high resolution XPS spectra of Bi, W, O, C were given in Fig. 3, respectively. The binding energy at 164.5 and 159.2 eV are corresponding to the Bi 4f7/2 and Bi 4f5/2 orbits of Bi^{3+}. After CQDs decoration, the binding energy of spin-orbit Bi 4f can be deconvoluted into two peaks at 164.7 and 159.4 eV, which is 0.2 eV higher than those of pristine Bi_2WO_6. For W element, the binding energy at 37.6 and 35.4 for pristine Bi_2WO_6 are corresponding to W 4f7/2 and W 4f5/2 assigning to the W^{6+} oxidation state, which shifts to higher 37.7 and 35.6 eV, respectively with CQDs decoration. The binding energy of O element in pristine Bi_2WO_6 can be deconvoluted into three peaks at 530.0, 530.6 and 532.1 eV, respectively, which corresponds to Bi—O, W—O and hydroxyl groups [20]. For CQDs2/Bi_2WO_6, the binding energies of O 1s orbits also display more or less higher energy shift. The binding energy shifts for elements Bi, W, O reflect the strong interaction between Bi_2WO_6 and CQDs. The binding energy of C1s orbits centered at 284.9, 285.8 and 288.8 eV assigns to C—C sp^2-hybridized carbon of CQDs, C—O and COO bond, respectively.

SEM images of pristine Bi_2WO_6 shows the nanoflake morphology which was aggregated with each other to form a hierarchical structure (Fig. S2). After a gentle wet impregnation of CQDs, the nanoflake aggregates structures were retained. TEM image of CQDs shows the high dispersion and uniform size of 3–5 nm in diameter (Fig. 4a and Fig. S3). We tried to get the HRTEM images of CQDs4/Bi_2WO_6 for demonstrating the presence of CQDs (graphitic carbon layer lattice) decorated on Bi_2WO_6 visually, while the process of HRTEM images capture reflects that it is difficult to get the exact information. HRTEM images of CQDs4/Bi_2WO_6 show that the contrast differences between CQDs and Bi_2WO_6 crystals is very fuzzy (Fig. 4b, Fig. S4), while nanoparticle-like substances (around 10 nm) appears under a relatively long time irradiation of electron beam (Fig. S4), which indicates that the possible decomposition of Bi_2WO_6 into Bi_2O_3 under high energy electron beam irradiation (Fig. S4). The above results may reflect that the high dispersion of CQDs on the hierarchical Bi_2WO_6 nanoflake aggregates.

The absorbance of UV–vis light is very important for photocatalysts. DRS UV–vis spectrum of pristine Bi_2WO_6 and CQDs decorated Bi_2WO_6 with different loading amounts were given in Fig. 5. The absorption of pristine Bi_2WO_6 start from 450 nm, the absorption edge gradually red shift to visible light region for CQD/Bi_2WO_6 composites with the increased amounts of CQDs. This result indicates the CQDs enhance the adsorption of visible light, which could improve the visible light photocatalytic activities.

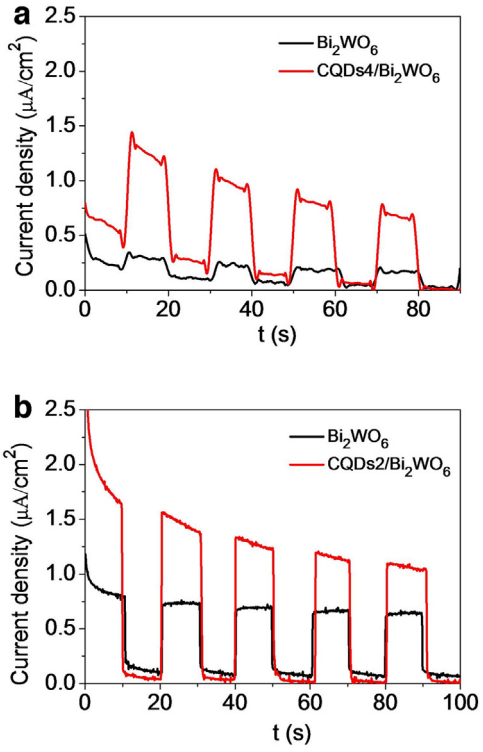

Fig. 6. The transient photocurrent density *vs.* t curves of pristine Bi_2WO_6 and CQD2/Bi_2WO_6 in 1 M Na_2SO_4 aqueous solution under visible ($\lambda > 420$ nm) and UV–vis light irradiation.

It is worthy to note that the absorption in UV region is maintained for CQDsx/Bi_2WO_6 (x = 1, 2, 3) in comparison with pristine Bi_2WO_6 except for CQDs4/Bi_2WO_6, which denotes that the shield effect of CQDs (orange color in ethanol) to UV light is limited with a low loading amount. This phenomenon should be benefit for the photocatalytic performance of CQDsx/Bi_2WO_6 (x = 1, 2, 3) in UV light region, wherein the CQDs can act as a positive role of electron acceptor. As shown in Fig. 6, the pristine Bi_2WO_6 and CQDx/Bi_2WO_6 photoelectrodes show transient photocurrent variation under light on/off alternations, which reveals that the photoelectrode fabricated on CQDx/Bi_2WO_6 nanocomposite possess higher photocurrents.

The gas-solid heterogeneous photocatalytic oxidation of VOCs was studied over photocatalysts of Bi_2WO_6 and CQDs/Bi_2WO_6 nanocomposite by evaluating the rate of CO_2 production. Typical gaseous polar acetone was used as probe organic pollutants, which was irradiated under visible light irradiations. Under visible light irradiation ($\lambda > 420$ nm), the blank experiment without photocatalysts shows that the acetone is rarely degraded within 8 h (Fig. 7), which indicates that the photolysis of acetone is difficult. In the presence of the pristine Bi_2WO_6, the acetone was gradually mineralized into CO_2 and the amounts of CO_2 *vs.* time shows linearly increasing tendency. The rate of CO_2 production is around 26.8 ppm/h over pristine Bi_2WO_6. In the presence of photocatalyst CQDsx/Bi_2WO_6 (x = 2, 3, 4), the rate of CO_2 production raises from 28 ppm/h to 47 ppm/h with increasing the content of CQDs, while a relative large amount of CQDs (CQDs6/Bi_2WO_6) results in the reduction of CO_2 production rate (26 ppm/h). It should be noted that the CQDs4/Bi_2WO_6 photocatalyst shows equivalent rate of CO_2 production in comparison with Pt/Bi_2WO_6 (48 ppm/h). The above results manifest that the decoration of CQDs greatly enhanced the photocatalytic oxidation efficiency of Bi_2WO_6.

Owing to the importance of stability for photocatalysts, the photocatalytic oxidation circling life of CQDs4/Bi_2WO_6 was evaluated

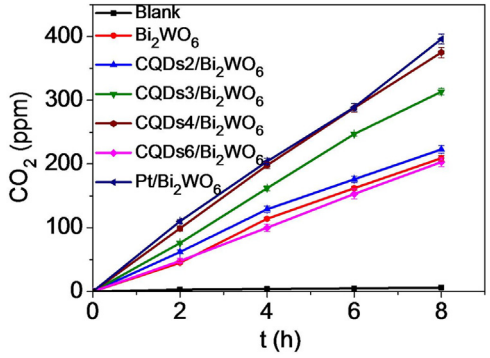

Fig. 7. CO_2 production during the photocatalytic oxidation of acetone in the presence of pristine Bi_2WO_6 and CQDs decorated Bi_2WO_6 nanoflake aggregates under visible light irradiation ($\lambda > 420$ nm).

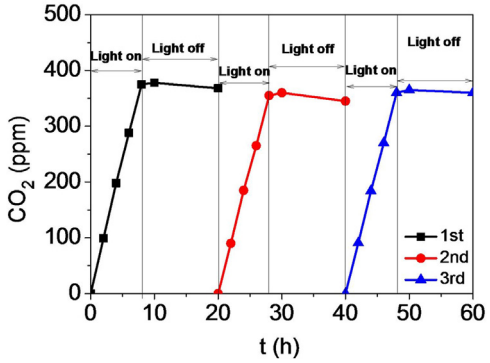

Fig. 8. Cycling runs of photocatalytic oxidation of acetone under UV–vis irradiation and dark condition alternatively.

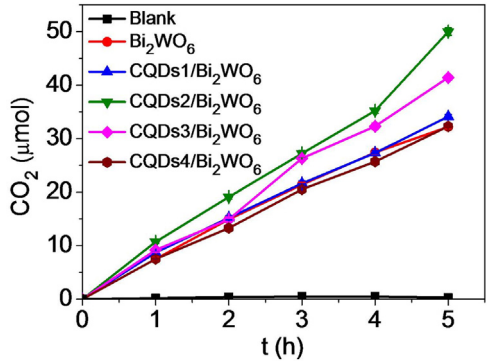

Fig. 9. Concentrations variations of CO_2 during the photocatalytic oxidation of acetone in the presence of pristine Bi_2WO_6 and CQDs decorated Bi_2WO_6 nanoflake aggregates under UV–vis light irradiation.

under visible light irradiation in the presence of gaseous acetone pollutant. The CO_2 production rate of first run over CQDs4/Bi_2WO_6 was around 48 ppm/h within 8 h, and a slight decrease was observed for the CO_2 production rate of second photo-oxidation run (47 ppm/h), which kept constant for the third run (Fig. 8). The circling life test indicates the high stability of CQDs4/Bi_2WO_6 composite.

The photocatalytic oxidation properties for gaseous acetone and toluene were also evaluated under UV light irradiation over Bi_2WO_4 and CQDs/Bi_2WO_4 photocatalysts. The CO_2 production from photolysis of acetone under UV–vis light is rarely observed within 5 h (Fig. 9). The decoration of CQDs on Bi_2WO_4 photocatalysts greatly improves the CO_2 production in comparison with that over pristine Bi_2WO_4. CQDs2/Bi_2WO_6 shows the highest CO_2 production

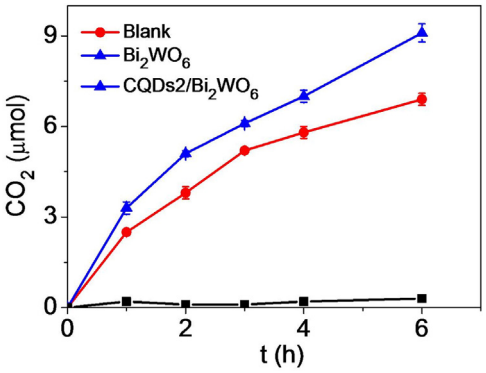

Fig. 10. The amounts of CO_2 released during the photocatalytic oxidation of toluene in the presence of pristine Bi_2WO_6 and CQDs decorated Bi_2WO_6 nanoflake aggregates under UV–vis light irradiation.

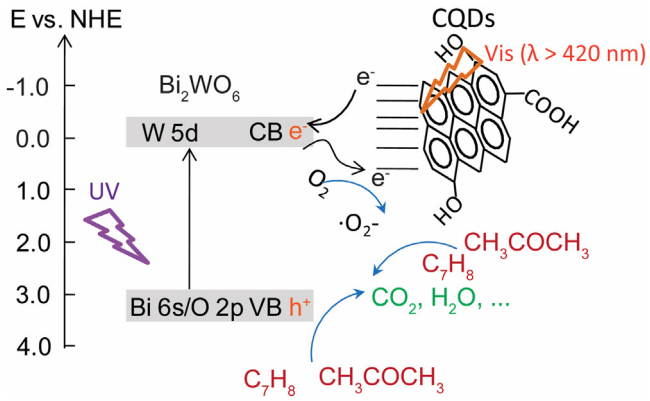

Fig. 11. The proposed mechanism of photocatalytic oxidation of VOCs upon CQDs/Bi_2WO_6 composite photocatalyst under UV–vis and visible light irradiation.

amount at every 1 h interval, and the CO_2 production amount over CQDs3/Bi_2WO_6 within 5 h is also larger than that over pristine Bi_2WO_4. CQDs1/Bi_2WO_6 shows comparable PCO activity with pristine Bi_2WO_4, while the CQDs4/Bi_2WO_6 with largest amount of CQDs shows slightly decreased CO_2 production amount at different time interval which may cause by the shield effect of CQDs toward UV light. The PCO performance is consistent with the photo-absorption properties of Bi_2WO_4 and CQDsx/Bi_2WO_6 photocatalysts. On the other hand, the CO_2 production of PCO of toluene over pristine Bi_2WO_4 and CQDs2/Bi_2WO_6 shows that the presence of CQDs greatly enhances the mineralization efficiency of toluene under UV irradiation (Fig. 10). The CO_2 production in PCO process of acetone increases linearly, while it increases quickly at first 1 h and then increase slowly in other 5 h for PCO process of toluene. This phenomenon should be related to the more complexity of PCO of toluene relative to that of acetone. It is well-established that the PCO of toluene undergoes the gradually oxidation of toluene into benzyl alcohol, benzaldehyde, bezenzoic acid, which results in the deactivation of photocatalyst due to the high chemical stability of these intermediates.

Based on the above results, Fig. 11 presents the proposed mechanism of photocatalytic oxidation of VOCs upon CQDs/Bi_2WO_6 composite photocatalyst. Bi_2WO_6 can be excited to form e^-/h^+ pairs under UV–vis and visible light irradiation. The h^+ is one of the strong oxidant for gaseous VOCs mineralization. On the other hand, a hybridized electronic structure coupled by CQDs and Bi_2WO_6, as well as the up-conversion properties of CQDs can contribute the red shift of light absorption and thus enhanced PCO performance especially under visible light irradiation. On the other hand, CQDs act as electron acceptors and donors, the electrons can be easily

transferred between CQDs and Bi_2WO_6 surfaces. Consequently, O_2 molecules adsorbed on surface of photocatalysts tend to form $^{\bullet}O_2^-$ and mineralize gaseous VOCs, which effectively inhibits the combination of the e^-/h^+. Finally, CQDs with aromatic rings decorated on Bi_2WO_6 may also be benefit to capture organic gaseous VOCs relative to pristine Bi_2WO_6.

4. Conclusions

In summary, electrochemically synthesized CQDs were facilely decorated on Bi_2WO_6 photocatalysts with controllable amount by a simple wet-impregnation method to form a hybrid CQDs/Bi_2WO_6 nanocomposite, which possess unchanged crystalline structure and morphology compared to pristine Bi_2WO_6. The light absorption of CQDs/Bi_2WO_6 displays red shifts due to the effective coupling of CQDs and Bi_2WO_6. The CQDs/Bi_2WO_6 nanocomposite exhibited enhanced visible and UV–vis light PCO of acetone and toluene into CO_2 via gas-solid reaction, which should be attributed to the accelerated charge separation and electron transfer due to electronic structure hybridization of CQDs and Bi_2WO_6. In all, the CQDs would be an promising candidate for smoothing electron transfer for those classic photocatalysts for gas-solid photocatalytic remediation of gaseous pollutants.

Acknowledgments

This work is supported by National Natural Science Foundation of China (21507083), Shanghai Government (15PJ1404000).

Appendix A. Supplementary data

Supplementary data associated with this article can be found, in the online version, at http://dx.doi.org/10.1016/j.apcatb.2016.04.009.

References

[1] J. Zhu, S.L. Wong, S. Cakmak, Environ. Sci. Technol. 47 (2013) 13276–13283.
[2] D.R. Gentner, D.R. Worton, G. Isaacman, L.C. Davis, T.R. Dallmann, E.C. Wood, S.C. Herndon, A.H. Goldstein, R.A. Harley, Environ. Sci. Technol. 47 (2013) 11837–11848.
[3] P. Thanh-Dong, B.-K. Lee, C.-H. Lee, Appl. Catal. B: Environ. 182 (2016) 172–183.
[4] C.L. Bianchi, S. Gatto, C. Pirola, A. Naldoni, A. Di Michele, G. Cerrato, V. Crocella, V. Capucci, Appl. Catal. B: Environ. 146 (2014) 123–130.
[5] D. Kibanova, J. Cervini-Silva, H. Destaillats, Appl. Catal. B: Environ. 43 (2009) 1500–1506.
[6] D. Yue, T. Zhang, M. Kan, X. Qian, Y. Zhao, Appl. Catal. B: Environ. 183 (2016) 1–7.
[7] Z. Bian, F. Cao, J. Zhu, H. Li, Environ. Sci. Technol. 49 (2015) 2418–2424.
[8] X. Qian, K. Fuku, Y. Kuwahara, T. Kamegawa, K. Mori, H. Yamashita, ChemSusChem 7 (2014) 1528–1536.
[9] X.F. Qian, T. Kamegawa, K. Mori, H.X. Li, H. Yamashita, J. Phys. Chem. C 117 (2013) 19544–19551.
[10] Y. Zhou, Y. Zhang, M. Lin, J. Long, Z. Zhang, H. Lin, J.C.S. Wu, X. Wang, Nat. Commun. 6 (2015) 1–8.
[11] L. Zhang, W. Wang, Z. Chen, L. Zhou, H. Xu, W. Zhu, J. Mater. Chem. 17 (2007) 2526–2532.
[12] C. Zhang, Y.F. Zhu, Chem. Mater. 17 (2005) 3537–3545.
[13] A. Rauf, M.S.A.S. Shah, G.H. Choi, U.B. Humayoun, D.H. Yoon, J.W. Bae, J. Park, W.-J. Kim, P.J. Yoo, ACS Sustain. Chem. Eng. 3 (2015) 2847–2855.
[14] Y. Peng, Q.-G. Chen, D. Wang, H.-Y. Zhou, A.-W. Xu, CrystEngComm 17 (2015) 569–576.
[15] X. Meng, Z. Zhang, J. Photochem. Photobiol. B 310 (2015) 33–44.
[16] H. Wang, L. Zhang, Z. Chen, J. Hu, S. Li, Z. Wang, J. Liu, X. Wang, Chem. Soc. Rev. 43 (2014) 5234–5244.
[17] D. Wang, L. Guo, Y. Zhen, L. Yue, G. Xue, F. Fu, J. Mater. Chem. A 2 (2014) 11716–11727.
[18] Y. Peng, M. Yan, Q.-G. Chen, C.-M. Fan, H.-Y. Zhou, A.-W. Xu, J. Mater. Chem. A 2 (2014) 8517–8524.
[19] Y. Tian, B. Chang, J. Lu, J. Fu, F. Xi, X. Dong, ACS Appl. Mater. Interfaces 5 (2013) 7079–7085.
[20] L. Yue, S. Wang, G. Shan, W. Wu, L. Qiang, L. Zhu, Appl. Catal. B: Environ. 176 (2015) 11–19.
[21] L. Ge, C. Han, J. Liu, Appl. Catal. B: Environ. 108 (2011) 100–107.
[22] E. Gao, W. Wang, M. Shang, J. Xu, Phys. Chem. Chem. Phys. 13 (2011) 2887–2893.
[23] S. Zhu, T. Xu, H. Fu, J. Zhao, Y. Zhu, Environ. Sci. Technol. 41 (2007) 6234–6239.
[24] J. Xia, J. Di, H. Li, H. Xu, H. Li, S. Guo, Appl. Catal. B: Environ. 181 (2016) 260–269.
[25] F. Deng, X. Lu, F. Zhong, X. Pei, X. Luo, S. Luo, D.D. Dionysiou, C. Au, Nanotechnology 27 (2016).
[26] J. Di, J. Xia, Y. Ge, H. Li, H. Ji, H. Xu, Q. Zhang, H. Li, M. Li, Appl. Catal. B: Environ. 168 (2015) 51–61.
[27] F. Nan, Z. Kang, J. Wang, M. Shen, L. Fang, Appl. Phys. Lett. 106 (2015).
[28] S. Fang, Y. Xia, K. Lv, Q. Li, J. Sun, M. Li, Appl. Catal. B: Environ. 185 (2016) 225–232.
[29] H. Zhang, H. Huang, H. Ming, H. Li, L. Zhang, Y. Liu, Z. Kang, J. Mater. Chem. 22 (2012) 10501–10506.
[30] D. Yan, Y. Liu, C.-y. Liu, Z.-y. Zhang, S.-d. Nie, RSC Adv. 6 (2016) 14306–14313.
[31] W. Donphai, T. Kamegawa, M. Chareonpanich, K. Nueangnoraj, H. Nishihara, T. Kyotani, H. Yamashit, Phys. Chem. Chem. Phys. 16 (2014) 25004–25007.
[32] T. An, J. Chen, X. Nie, G. Li, H. Zhang, X. Liu, H. Zhao, ACS Appl. Mater. Interfaces 4 (2012) 5988–5996.
[33] N. Bouazza, M. Ouzzine, M.A. Lillo-Rodenas, D. Eder, A. Linares-Solano, Appl. Catal. B: Environ. 92 (2009) 377–383.
[34] H. Li, X. He, Z. Kang, H. Huang, Y. Liu, J. Liu, S. Lian, C.H.A. Tsang, X. Yang, S.-T. Lee, Angew. Chem. Int. Ed. 49 (2010) 4430–4434.
[35] H. Yu, Y. Zhao, C. Zhou, L. Shang, Y. Peng, Y. Cao, L.-Z. Wu, C.-H. Tung, T. Zhang, J. Mater. Chem. A 2 (2014) 3344–3351.
[36] M. Qamar, R.B. Elsayed, K.R. Alhooshani, M.I. Ahmed, D.W. Bahemann, ACS Appl. Mater. Interfaces 7 (2015) 1257–1269.